https://doi.org/10.46813/2026-165-127

EFFECT OF A TUBULAR HIGH-CURRENT RELATIVISTIC ELECTRON BEAM ON THE GRAIN STRUCTURE OF GRANITE

S.E. Donets[1], V.V. Lytvynenko[1,2], V.V. Shatov[1], O.L. Rak[2]
[1]Institute of Electrophysics and Radiation Technologies NAS of Ukraine, Kharkiv, Ukraine;
[2] National Science Center "Kharkiv Institute of Physics and Technology", Kharkiv, Ukraine
E-mail: sjd458@ukr.net

This paper examines the structural features of a red granite sample irradiated with a high-current electron beam. The significance of the data obtained is substantiated for assessing the stability of granites as potential barriers in the long-term disposal of radioactive waste, as well as for other radiation-technological applications. A statistical comparison of grain size and shape in the irradiated and non-irradiated regions of the granite is performed. The software developed for the statistical analysis of optical microscopy data is described. A physical model of granite failure under the action of a high-power electron beam is proposed.

PACS: 52.40.HF, 29.27Ac, 621.715:539.376, 87.55N

INTRODUCTION

Reducing greenhouse-gas emissions entails the search for unconventional energy sources, in particular the extraction of gaseous hydrocarbons for subsequent use in hydrogen production. The deposits currently being developed lie at great depths, so unconventional tools such as concentrated electrophysical energy flows are being considered for their efficient extraction. For example, in patent [1] an electron beam was proposed as a means of carrying out mining operations; the failure mechanism there was the ablative ejection of material under the pressure that builds up in the electron thermalization zone and causes a corresponding temperature rise. A comprehensive analysis of the possibility of using high-power lasers for tunneling operations is given in [2]; the drawbacks noted include the low efficiency of energy use and the small penetration depth, which reduces the specific material removal per unit of energy invested. In [3], the patterns of granite mass removal as a function of the absorbed laser energy were investigated, together with the effect of the distance from the radiation source on the size of the failure zone of the granite target.

Another area of application of high-power electron beams is the introduction of radiation-thermal processes for treating raw materials for the cement industry, which makes it possible to reduce emissions from hydrocarbon combustion and to increase production efficiency [4]. A technology for rock failure under the action of high-voltage discharges is considered in [5]. The shapes of the voltage and current pulses were established as functions of the initial battery energy and of the water, air, and solid-phase content of the material being processed. In [6], a number of engineering solutions are proposed for the use of a pulsed electron beam in tunneling operations during tunnel construction, and the possibility of accelerating the work by using electron beams with frequency-switching capability was established. In discussing the effects of electron-beam interaction with rock, the problem of the long-term disposal of radioactive waste [7, 8] should also be noted, since it requires an assessment of the stability of natural minerals against fluxes of ionizing radiation of various intensities. Given that, at the current stage of nuclear power development, most radioactive waste (from which the actinides will not be removed) will be stored for more than a thousand years, many factors affecting the rock massif as a whole must be taken into account: lightning strikes, explosions caused by military action (nuclear explosions should not be ruled out either), earthquakes, aircraft crashes, and meteorite impacts. AI-based monitoring platforms [9] are currently being developed to track the state of rock massifs in which radioactive waste is disposed of. Such an approach relies on a set of physical models describing the state of the system, so that the combined electromagnetic, shock, radiation, and thermal effects must be reproduced. In [10, 11] we showed that a high-current relativistic electron beam (HCREB) acting on metal targets is able to reproduce this set of effects. In the case of mineral irradiation, at least some change should be expected in the factors governing both the spatial distribution of the absorbed dose and the failure mechanisms of the target. The validity of this assumption is confirmed by the data of [12], in which grain orientation and size were studied in the assessment of the resistance of granites to crack propagation.

1. EXPERIMENTAL PROCEDURE

A pink granite sample was irradiated with a single electron-beam pulse with the following parameters: electron energy 350 keV, beam current 2 kA, pulse rise time 5 μs. The beam had an annular cross-section, with a diameter of 60 mm and a wall thickness of about 5 mm. Irradiation was carried out in vacuum. Prior to irradiation, the samples were held in a drying oven at 50 °C. The microstructure of the granite was analysed by optical microscopy, with subsequent image processing using in-house software.

2. RESULTS AND DISCUSSION

In analysing the mechanism of crater formation in granite under HCREB irradiation, it should be noted that this mechanism differs somewhat from that operating in metal targets. As in metal targets, failure occurs through the contribution of the thermoelastic effect, which at a certain instant exceeds the strength limit of the material. At the same time, granite is a dielectric, so that electron thermalization is accompanied by the accumulation of electric charge, which forms an electrostatic field and

thereby gives rise to an additional failure mechanism. The condition for granite failure is therefore that the sum of the stresses due to the thermoelastic effect F_T, the electrostatic interaction forces F_{el}, and the internal stresses F_{in} exceed the strength limit at a given temperature σ, which may be described in general by the expression

$$F \le F_T + F_{el} + F_{in}, \quad (1)$$

where $F_T = \frac{\Delta T \cdot C}{\alpha \cdot T}$, α is the coefficient of thermal expansion, C is the heat capacity

$$F_{el} = \frac{n^2 \cdot e^2}{V \cdot \varepsilon} \cdot \exp\left(-\frac{\sigma}{\varepsilon \cdot \varepsilon_0}\right),$$

V is the volume of the electric-charge distribution, ε is the dielectric constant; n is the number of free elementary charges; e is the elementary charge; σ is the electrical conductivity; ε is the dielectric permittivity.

The determining factor is the dynamics of the temperature field, since the conductivity of granite increases sharply with rising temperature and with crack formation. It should be borne in mind, however, that at the initial stage of irradiation the electric charge that accumulates acts as a factor providing additional stopping power in the material.

Since the irradiation pulse duration is comparable to the acoustic relaxation time, the volume in which the electron-beam energy is absorbed has no time to expand, which induces a compressive stress leading to spallation of the near-surface region of the irradiated sample. As a result, two thermoelastic waves, one of compression and one of rarefaction, propagate from the irradiated volume in opposite directions.

Fig. 1 shows a sample of red medium-grained granite irradiated with a single pulse of a tubular electron beam, which produced an annular crater approximately 0.3 mm deep.

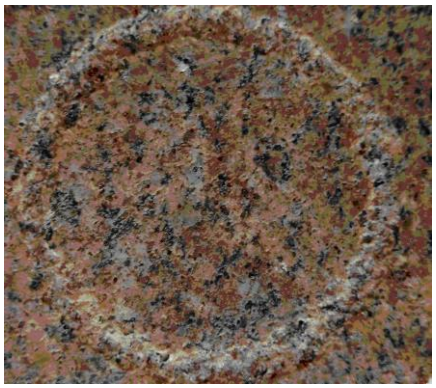


Fig. 1. A sample of red granite irradiated with an electron-beam pulse

In assessing the mechanisms of granite failure, most researchers regard the onset of melting along grain boundaries as the basis of the process [1, 13], with the pressure of the evolved gases acting as an additional driving force for ejection.

Since the irradiation pulse duration is comparable to the acoustic relaxation time, the volume in which the electron-beam energy is absorbed has no time to expand, which induces a compressive stress leading to spallation of the near-surface region of the irradiated sample. As a result, two thermoelastic waves, one of compression and one of rarefaction, propagate from the irradiated volume in opposite directions. Fig. 2 presents optical microscopy data for the surface of the non-irradiated and irradiated regions of the target.

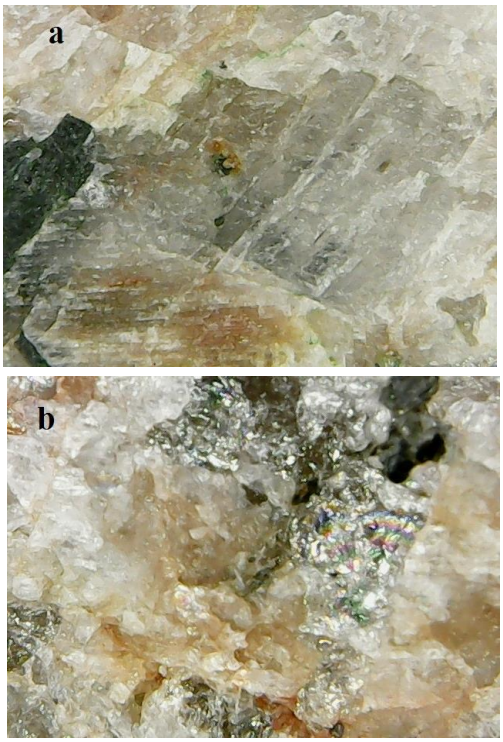


Fig. 2. Optical microscopy images of the non-irradiated (a) and irradiated (b) regions of the target (50× magnification)

Understanding the contribution of these processes is important in view of all the practical aspects of work with granites noted above, such as mineral extraction from granite deposits, the use of granite massifs for the long-term disposal of radioactive waste, and other mining operations. Thus, the development of cracks in granite at various temperatures and pressures is investigated in [14], while in [15] the fragmentation of granite by gas flows was considered as an alternative to hydraulic fracturing. It is notable that in both studies the grain structure was examined by means of colour segmentation of the grains. Fig. 3 provides a clearer demonstration of the difference in grain structure between the initial and the irradiated regions: irradiation causes grain refinement and reveals new crystallite formations that had previously been incorporated into larger clusters during the primary formation of the material. The proposed algorithm combines the Segment Anything Model (SAM) [16], a foundation model for image segmentation, with classical methods of mathematical morphology. This hybrid approach is motivated by the fact that SAM provides reliable zero-shot object detection, that is, without additional training on petrographic images, although the contours it produces are only approximately localized; classical methods, by contrast, provide sub-pixel boundary accuracy but require reliable initialization. Processing is carried out in five stages.

At the first stage, the image is fed to the SAM encoder, which is built on the Vision Transformer architecture [17] and pre-trained by masked autoencoding [18]. In automatic mask-generation mode, a uniform grid of point prompts (32×32 by default) is distributed over the image, and for each prompt the decoder predicts up to three candidate masks of different scale together with a quality score.

At the second stage, the set of overlapping masks is converted into an unambiguous label map in which each pixel corresponds to one and only one grain identifier. The masks are ordered by increasing area, and each pixel is assigned to the smallest (most specific) mask covering it. At the third stage, the boundaries are refined by marker-controlled watershed segmentation; for grains thinner than the structuring element, a non-eroded mask is used to prevent their loss.

At the fourth stage, morphometric characteristics are computed for each grain from image moments [19].

At the fifth stage, a report is generated comprising raster images of the boundaries and of the segmentation results, a table of characteristics in CSV format, a label map in the form of an integer array, and an interactive HTML report with a sortable table. An optional manual-correction mode is provided, in which the operator can merge erroneously split grains or separate merged ones by means of a SAM point prompt.

The algorithm is implemented in Python using the PyTorch [20] and scikit-image [21] libraries, with automatic selection of the computing device. The PyTorch build is chosen according to the highest CUDA version supported by the installed driver. Running the image encoder on a GPU yields a speed-up of one to two orders of magnitude relative to a CPU, in agreement with the theoretical estimate: the dominant component is the matrix multiplication of the attention mechanism [22], which has a complexity of $O(n^2d)$ and a high arithmetic intensity and therefore makes efficient use of the parallel architecture of the GPU. The quantitative results of the processing are given in Table.

Quantitative results of segmentation

Parameter	**Irradiated sample**	**Non-irradiated sample**
Mean grain area, px²	1,005.0	1,444.0
Median grain area, px²	304.0	163.0
Min./max. area, px²	1 / 19,958	1 / 162,876
Mean equivalent diameter, px	26.97	23.18
Mean eccentricity	0.755	0.799

Comparison of the irradiated and non-irradiated regions shows that the action of the pulsed electron beam causes a rearrangement of the grain structure of the granite: large grain clusters are broken up, the mean grain area decreases, and the maximum grain size is substantially reduced. The simultaneous increase in the median area and in the mean equivalent diameter indicates a redistribution of grain sizes after irradiation, while the decrease in eccentricity indicates a tendency towards the formation of less elongated fragments. This confirms that the failure of granite under HCREB action is not only thermal but also structural-mechanical in nature, being associated with fragmentation and with the opening of grain boundaries.

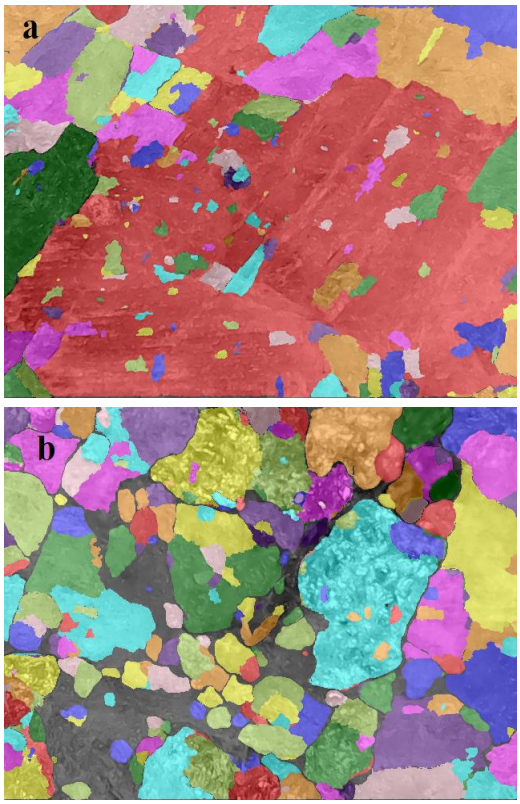


Fig. 3. Images of the non-irradiated (a) and irradiated (b) regions of the target processed by the image-segmentation method

The evolution of the temperature-field distribution was computed by finite-difference methods. The differential-difference problem was solved using the Crank–Nicolson scheme on an orthogonal unstructured grid that we had tested previously in [23]. The classical Fourier equation for heat conduction in solids has the unphysical property of allowing thermal waves to propagate in a medium at an arbitrary velocity. Therefore, given the high heating rates and the pressure values involved, it is considered necessary to take into account the relaxation time τ_r, which reflects the finite propagation velocity of the temperature field in the material, by using the relaxation heat-conduction equation

$$\bar{q}(x,t+\tau_r) = -k\nabla T(x,t) - \tau_r \frac{\partial \bar{q}}{\partial t} - k\tau\nabla_r \frac{\partial T}{\partial t}, \qquad (2)$$

where $q(x,t) = W_m \cdot \exp\left[-\left(\frac{x-x_m}{2x_m}\right)^2\right]$ distribution of the heat source function along the coordinate x extending into the target; x_m – coordinate corresponding to the energy absorption maximum; k – thermal diffusivity; $W_m = \frac{U \cdot I \cdot \tau}{\rho \cdot S}$ – maximum of absorbed radiation energy; I is the primary-electron current; U is the electron energy, and the backscattering coefficient is taken into account.

Under HCREB irradiation, the temperature rise removes the influence of the non-uniform topology of grain orientation and leads to more intensive removal of the target material. The spatio-temporal distribution of the temperature field is shown in Fig. 4.

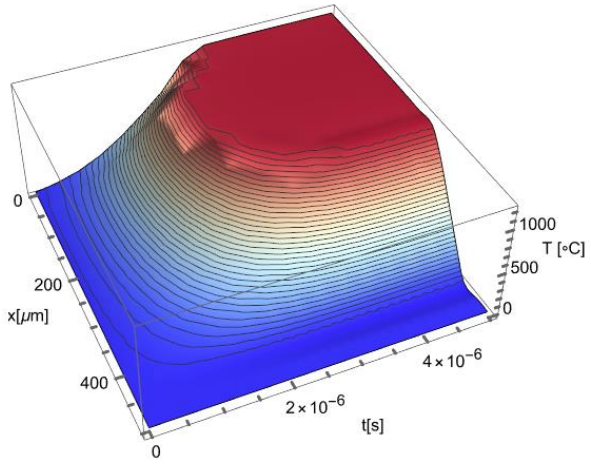


Fig. 4. Distribution of the temperature field during single-pulse irradiation, calculated up to 5 μs after the onset of the pulse. Here x is the penetration depth into the granite and T is the temperature

The melting temperature was reached approximately 2 μs after the onset of irradiation. The maximum penetration of the beam into the bulk of the material was calculated to be about 400 μm for a single pulse, which is smaller than the mean grain size of about 1 mm. Notably, the calculated extent of melting reached 220…330 μm during a single pulse, depending on variations in the irradiation density. When this is compared with the crater depth of ~0.4 mm produced by one pulse, melting cannot be the sole dominant mechanism. This could not be attributed to variations in the beam density at the target. It therefore appears that cracking contributes substantially to ablation, comparably to the formation of the melt cavity. Transgranular cracking is assumed to have occurred, in particular along pre-existing defects. Intergranular cracking also took place, but probably at later stages, as the thermal wave propagated into the bulk. The shock wave may likewise have led to the formation or the consumption of an extensive crack network, which could have contributed to the surface damage.

CONCLUSIONS

The changes induced in granite by a high-current relativistic electron beam can help to elucidate processes whose understanding is important for a number of technological applications. Modern approaches to the disposal of long-lived radioactive waste in rock massifs involve the use of artificial-intelligence tools for monitoring the state of the barrier material. One component of this task is the identification of changes in the grain structure, for which computational image-segmentation procedures applied to microscopy data may be employed. The study demonstrates that segmentation can serve as the basis for computer-aided procedures to analyze changes in the grain structure of irradiated granite. Based on the construction of a thermal field model, it is confirmed that thermal expansion is the primary mechanism of granite degradation under electron beam irradiation. The role of the electric charge accumulating during the irradiation pulse requires further investigation.

REFERENCES

1. Stirling A. Colgate, Socorro N. Mex. Methods of mining rock with an electron beam // *USA Patent*. 1977, 4,020,317.

2. R.P. Madavi, R. Mitra, P. Diwakar. Laser-Induced Rock Breakage (LIRB) Technology in Mining Engineering - A Review // *Paper presented at the 58th U.S. Rock Mechanics Geomechanics Symposium*, Golden, Colorado, USA, June 2024, Paper Number: ARMA-2024-1081; https://doi.org/10.56952/ARMA-2024-1081

3. Chenguang Guo, Yu Sun, Haitao Yue, Qiang Li, Shunzhi He, Jianzhuo Zhang, Yin Zhang. Experimental research on laser thermal rock breaking and optimization of the process parameters // *International Journal of Rock Mechanics and Mining Sciences*. 2022, v. 160, p. 105251; https://doi.org/10.1016/j.ijrmms.2022.105251

4. I.G. Abramson, G.B. Egorov, and Yu.V. Nikiforov. The Design of Pilot Line for Cement Clinker Production by RT-technology // *The 5th International Symposium on Cement and Concrete/ Shanghai*. 2002, p. 56-60.

5. C. Li, L. Duan, S. Tan, V. Chikhotkin. Influences on High-Voltage Electro Pulse Boring in Granite // *Energies*. 2018, v. 11, p. 2461; doi:10.3390/en11092461

6. R.T. Avery, D. Keefe, T.L. Brekke, I. Finnie. Hard rock tunneling using pulsed electron beam // *IEEE Transaction on Nuclear Science*. 1975, v. NS-22, N 3, p. 1798-1801.

7. V.F. Klepikov, E.M. Prokhorenko, V.V. Lytvynenko, S.E. Donets, V.N. Robuk, T.G. Prokhorenko, V.T. Uvarov, A.G. Ponomarev, Yu.F. Lonin. The use of high-current relativistic electron beams for the study of the effects of ionizing radiation on materials storage RAW // *Problems of Atomic Science and Technology*. 2016, N 2(102), p. 72-77.

8. Yu. Olkhovyk. Geological storage of highly active waste in Ukraine: problems and prospect of construction // *Geochemistry of Technogenesis.* 2020, N 4, p. 15-22; https://doi.org/10.15407/geotech2020.32.015

9. Olaf Kolditz et al. Digitalisation for nuclear waste management: predisposal and disposal // *Environmental Earth Sciences*. 2023, v. 82, p. 42; https://doi.org/10.1007/s12665-022-10675-4

10. V.V. Bryukhovetsky, V.F. Klepikov, V.V. Lytvynenko, D.E. Myla, Yu.F. Lonin, A.G. Ponomarev. The Structural Phase State and Strength Properties of the Surface Layer of AA6111-T4 Aluminum Alloy Irradiated by the High-Current Electron Beam // *Nuclear Inst. and Methods in Physics Research B*. 2022, v. 519, p. 1-8; https://doi.org/10.1016/j.nimb.2022.03.008

11. V.V. Bryukhovetsky, V.V. Lytvynenko, O.A. Startsev, D.E. Myla, Yu.N. Volkov, O.L. Rak. Mechanisms of deformation induced by high-current pulsed electron beam irradiation // *Materials Letters*. 2024, v. 367, p. 136642; https://doi.org/10.1016/j.matlet.2024.136642

12. H. Rezaee, M. Noorian-Bidgoli. Numerical and experimental investigations of grain size and temperature effects on the crack propagation velocity in brittle rocks // *Computational Particle Mechanics*. 2025, v. 12, p. 2969-2981; https://doi.org/10.1007/s40571-025-00962-9

13. B.W Chappell, A.J.R White, D.Wyborn. The Importance of Residual Source Material (Restite) in Granite Petrogenesis // *J. Petrology*. 1987, v. 28, N 6, p. 1111-1138.

14. Lei Wang et al. Effects of temperature and confining pressure on the permeability of Beishan granite from high-level radioactive waste disposal Repository // *Case Studies in Thermal Engineering*. 2024, v. 55, p. 104111; https://doi.org/10.1016/j.csite.2024.104111

15. Xiting Long et al. Gas fracturing behavior and breakdown pressure prediction model for granite under different confining pressure and injection rate // *Geomech. Geophys. Geoenerg. Georesour*. 2023, v. 9, p. 76; https://doi.org/10.1007/s40948-023-00623-2

16. A. Kirillov, E. Mintun, N. Ravi, et al. Segment Anything *// Proc. IEEE/CVF Int. Conf. on Computer Vision (ICCV).* 2023, p. 4015-4026; https://doi.org/10.1109/ICCV51070.2023.00371

17. A. Dosovitskiy, L. Beyer, A. Kolesnikov, et al. An Image is Worth 16x16 Words: Transformers for Image Recognition at Scale // *Int. Conf. on Learning Representations (ICLR),* 2021; https://doi.org/10.48550/arXiv.2010.11929

18. K. He, X. Chen, S. Xie, et al. Masked Autoencoders Are Scalable Vision Learners // *Proc. IEEE/CVF Conf. on Computer Vision and Pattern Recognition (CVPR)*. 2022, p. 16000-16009; https://doi.org/10.1109/CVPR52688.2022.01553

19. M.-K. Hu. Visual Pattern Recognition by Moment Invariants // *IRE Trans. on Information Theory.* 1962, v. 8, N 2, p. 179-187.

20. A. Paszke, S. Gross, F.Massa, et al. PyTorch: An Imperative Style, High-Performance Deep Learning Library // *Advances in Neural Information Processing Systems (NeurIPS),* 2019; https://doi.org/10.48550/arXiv.1912.01703

21. S. Van der Walt, J.L. Schönberger, J. Nunez-Iglesias, et al. Scikit-image: Image Processing in Python *// Peer J*. 2014, v. 2, e453.

22. A. Vaswani, N. Shazeer, N. Parmar, et al. Attention is all You Need // *Advances in Neural Information Processing Systems (NeurIPS),* 2017, p. 5998-6008; https://doi.org/10.48550/arXiv.1706.03762

23. A.G. Kobets, P.R. Horodek, O.A. Startsev, et al. Melting effect on high current electron beam on aluminum alloy 1933 // *Surface Engineering and Applied Electrochemistry*. 2015, v. l51, N 5, p. 478-482; DOI: 10.3103/S1068375515050075

Article received 14.09.2026

ВПЛИВ ТРУБЧАСТОГО СИЛЬНОСТРУМОВОГО РЕЛЯТИВІСТСЬКОГО ЕЛЕКТРОННОГО ПУЧКА НА ЗЕРЕННУ СТРУКТУРУ ГРАНІТУ

С.Є. Донець, В.В. Литвиненко, В.В. Шатов, О.Л. Рак

Вивчено особливості будови зразка червоного граніту, опроміненого сильнострумовим електронним пучком. Обгрунтовується важливість здобутих даних для оцінки стійкості гранітів як потенційних бар'єрів при довготривалому захороненні радіоактивних відходів, а також для інших радіаційно-технологічних застосувань. Здійснено статистичне порівняння розмірів та форми зерен опроміненої та неопроміненої ділянок граніту. Наведено опис програмного забезпечення для проведення статистичного аналізу даних оптичної мікроскопії. Запропонована фізична модель руйнування граніту під впливом потужного електронного пучка.